RESEARCH ARTICLE | AUGUST 18 2023

Applications of the Petra-M simulation code for the magnetospheric physics

E.-H. Kim ✉; S. Shiraiwa; N. Bertelli; C. Z. Cheng; M. Ono; K. S. Park; J. R. Johnson

AIP Conf. Proc. 2984, 130001 (2023)
https://doi.org/10.1063/5.0164070

Applications of the Petra-M Simulation Code for the Magnetospheric Physics

E.-H. Kim,[1, a)] S. Shiraiwa,[1] N. Bertelli,[1] C. Z. Cheng,[1] M. Ono,[1] K. S. Park,[2] and J. R. Johnson[3]

[1)] *Princeton Plasma Physics Laboratory, Princeton University, Princeton, NJ, USA.*
[2)] *Department of Astronomy and Space Science, Chungbuk National University, Cheongju, South Korea.*
[3)] *School of Engineering, Andrews University, Berrien Springs, MI, USA.*

[a)] *Corresponding author: ehkim@pppl.gov*

Abstract.
We present applications of the full-wave solver, Petra-M code for Earth magnetospheric plasma wave physics by leveraging the current effort of the radio frequency wave project. Because the Petra-M code uses the modular finite element method (MFEM) library, the boundary shapes, plasma density profiles, and realistic planetary magnetic fields can be easily adapted. In order to incorporate realistic Earth's magnetic field into the Petra-M, we utilize the self-consistent magnetospheric flux models for compressed and stretched magnetic fields and realistic magnetospheric magnetic field geometries extracted from global MHD simulations. Using Petra-M code, we then examine ultra-low frequency (ULF) wave propagations in various magnetic field shapes. For example, left-handed polarized electromagnetic ion cyclotron waves in Earth's dipole and compressed magnetic field are examined to consider waves in the inner and dayside outer magnetospheres, respectively. Mode-converted Alfvén wave propagation is also demonstrated in the compressed (dayside), stretched(nightside), and realistically stretched magnetic field (magnetotail). Therefore, the Petra-M code successfully demonstrates magnetospheric plasma wave propagation despite the spatial scale differences between the fusion devices ($\sim$ m) and Earth's magnetosphere ($10^3 - 10^4$km).

INTRODUCTION

The solar wind's interaction with the Earth's magnetic field causes many intriguing phenomena. Due to the action of the solar wind, Earth's magnetic field is compressed on the dayside and stretched on the night side, respectively, and dawn-dusk asymmetry can also appear. In addition to the solar wind activities, the tilted Earth's magnetic field also can affect magnetospheric configurations.

Ultra-low frequency (ULF) waves (< 5 Hz, lower than the proton ion cyclotron frequency) are a prominent feature of the Earth's magnetosphere and ionosphere. Since ULF waves, including Alfvén and electromagnetic ion cyclotron (EMIC) waves, interact with magnetospheric electrons and ions [1, 2, 3], understanding the plasma wave spatial distribution under various plasma conditions is essential for magnetospheric physics.

Many theoretical efforts have examined ULF waves using simulation tools, such as ray tracing codes [4], MHD wave codes in orthogonal [5] and non-orthogonal dipole coordinates [6], hybrid wave codes [7], gyrofluid-kinetic electron model [8], time-dependent multi-fluid wave code in a slab coordinate [9], 1D [10] and 2D [11] full-wave codes in multi-fluid plasma. These simulation codes successfully demonstrate ULF waves in Earth's magnetosphere, such as field line resonance [5] and ion-ion hybrid resonance [9] and generation and propagation of left-handed polarized (LHP) EMIC waves [7, 11]; however, realistic magnetospheric configurations cannot be easily adopted into most existing codes, except ray tracing code and full-wave code using the finite element (FEM) methods. Although the ray tracing method is one of the first steps in examining the wave properties, it cannot describe the detailed wave properties of cutoff, mode conversion, or polarization reversal. Full-wave simulations can overcome the weakness of the ray tracing method and fully describe wave phenomena. One of the advantages of the simulation code using FEM is that the boundary shapes, plasma density profiles, and magnetic field configurations are readily adapted; therefore, a 2D full-wave code (FW2D) using the FEM method has been developed at the PPPL and is applied to various magnetic field configurations, such as Mercury and Earth's magnetospheres and NSTX [12, 13, 14].

In this paper, we adopt an advanced full-wave solver based on FEM, Petra-M, rather than the previous FW2D code for applications to space plasmas in complex geometries. To verify the Petra-M code in magnetospheric physics, we first adopt the dipole magnetic field, which is primarily valid for the inner magnetosphere. Due to solar wind compression, Earth's magnetic field lines are compressed on the dayside and stretched on the night side. Such shapes are described in an Euler potential magnetic field model [15] and a self-consistent magnetospheric flux model [16]. We utilize these models in the Petra-M and also use realistic magnetospheric magnetic field configurations extracted from a global MHD simulation [17] into the Petra-M code.

24th Topical Conference on Radio-frequency Power in Plasmas
AIP Conf. Proc. 2984, 130001-1–130001-6; https://doi.org/10.1063/5.0164070
Published by AIP Publishing. 978-0-7354-4604-5/$30.00

We then examine the left-handed polarized (LHP) EMIC wave propagation in dipole and compressed magnetic fields. Wave simulations of MHD waves are also performed in compressed and stretched magnetic fields and realistic magnetic fields extracted from the global MHD simulation.

PETRA-M CODE FOR THE MAGNETOSPHERIC WAVES

We adopt a state-of-the-art full-wave simulation tool, Petra-M, to model plasma wave propagation in cold plasma [18, 19]. The newer advanced Petra-M code can provide more accurate solutions and better user interfaces than the FW2D [11]. The Petra-M code uses the modular finite element method (MFEM) library developed at Lawrence Livermore National Laboratory for finite element discretization. The Petra-M code has been used to successfully model plasma waves in various tokamak machines using 2D/3D simulations [20, 21, 22]. A graphical user interface is prepared in πScope, where users can set domain and boundary conditions. Therefore, for 2D simulations, we can generate triangular meshes given a specified boundary and a target density function. Then, we define the dielectric tensor using the given plasma density and magnetic field topology and add it to the code. The code computes the electric field when these wave modes are launched from a wave source and can be used to examine the resulting distribution of wave characteristics, such as polarization, the direction of Poynting flux, and wave absorption at relevant, resonant surfaces.

Similar to other wave models in the magnetosphere [5, 11], we assume a quasi-stationary state of multi-ion space plasma in which background plasma flow speed can be ignored relative to the fluctuation speed. Space plasma does not have physical outer metal boundaries and no antenna-generating waves except in artificial experiments. Therefore, we limited the simulation domain near the target location and added intense collisions near the outer boundary to express outgoing waves at the boundary. We assumed waves were generated at the source location with specific wave frequency and polarization status according to generation theories.

Because the spatial scales of planetary magnetospheres (10^3 – 10^4 km) are extremely large compared to the scales of the laboratory plasmas ($\sim$ m) that Petra-M currently considers, the spatial differences in the Petra-M model were re-scaled to an Earth's radii (R_E), which is similar to the FW2D code. We then adopt a dipole geometry, compressed magnetic field in the dayside magnetosphere, and stretched magnetic field in the nightside magnetosphere. We also adopt a plasma configuration extracted from a global MHD simulation.

The dipole magnetic field in cylindrical coordinates (r, z, ϕ) can be derived as,

$$B_0 = \frac{B_S}{R^3}\sqrt{1+3\sin^2\lambda_M}, \quad (\hat{b}_r, \hat{b}_z, \hat{b}_\phi) = \left(\frac{-3\sin\lambda_M\cos\lambda_M}{1+\sin^2\lambda_M}, \frac{1-3\sin^2\lambda_M}{1+\sin^2\lambda_M}, 0\right), \tag{1}$$

where B_0, $\hat{b}_r$, $\hat{b}_z$ and $\hat{b}_\phi$ are magnetic field strength, magnetic field unit vector in r, z, and ϕ direction, and R, B_s and λ_M are a geocentric radial distance, background magnetic field strength at the surface, and magnetic latitude, respectively. Magnetic latitude in each grid point can be calculated $\lambda = \tan^{-1}(z/r)$; thus, $\hat{b}_r$, $\hat{b}_z$, $\hat{b}_\phi$ and B_0 are easily calculated in the Petra-M module as shown in Figure 1(a).

For the compressed and stretched magnetic field topologies, we first adopt an Euler potential magnetic field model [15] (hereafter Stern's model). Magnetic fields can be represented by the cross-product of the gradients of two scalars (α and β), such as Euler potentials,

$$B_0 = \nabla\alpha \times \nabla\beta. \tag{2}$$

Using equations (43) and (44) in Stern [15], $\nabla\alpha$ and $\nabla\beta$ can be calculated, and we developed a module calculating $\hat{b}_r$, $\hat{b}_z$, $\hat{b}_\phi$, and B_0, in the Petra-M code. Figure 1(b) presents the calculated compressed magnetic field flux tube and the magnetic field strength.

We also adopted a self-consistent magnetospheric equilibrium code, the MAG2D code, which has been previously developed at PPPL [16]. We calculate each magnetic field $\mathbf{B}_0(\alpha,\beta)$ in the magnetic flux coordinate by adopting the detected disturbance storm time index, solar wind pressure, and interplanetary magnetic field strength. The spatial position (x, z) of each magnetic flux coordinate is calculated: thus, MAG2D generates (B_0, $\hat{b}_r$, $\hat{b}_z$, $\hat{b}_\phi$) at $(x(\alpha,\beta), z(\alpha,\beta))$, as shown in Figure 1(c–d). We interpolated the magnetic field computed in MAG2D at each node of the Petra-M generated mesh. For dipole, Stern, and MAG2D models, we adopt an empirical electron density model [23],

$$N_e = 1390\left(\frac{3}{L}\right)^{4.83}\left(\frac{L}{R/R_E}\right)^{0.8}, \tag{3}$$

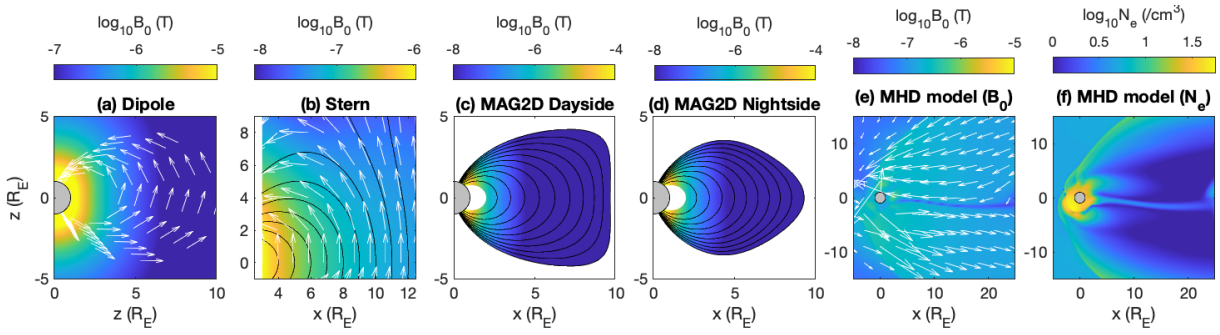

FIGURE 1: Various magnetic field configurations we adopted in the Petra-M; (a) Dipole model from equation (1), (b) Stern model [15], (c-d) MAG2D model [16], and (e-f) global MHD simulations [17]. Here, black lines and white arrows represent the flux line and magnetic field direction, respectively.

where L is L-shell number which can be defined $L = R/R_E \cos^2 \lambda_M$ in dipolar magnetic field line.

Finally, we adopt realistic magnetic field geometries from a global MHD simulation [17] into the Petra-M code. For 2D simulations, we consider a meridional slice of the magnetosphere in 3D MHD simulations, as shown in Figure 1(e), and extract a spatial time snapshot of magnetic field topologies and density profiles from the time-dependent global MHD simulations.

ULF WAVE SIMULATIONS

Electromagnetic ion cyclotron (EMIC) wave propagation

The EMIC waves in the Pc 1-2 frequency range (0.1-5Hz) are often detected from the Earth's magnetosphere-ionosphere. The EMIC waves are known to be excited as LHP waves near the magnetic equator by anisotropic protons, and ground-based magnetometers often detect these waves [24]. One of the critical scientific questions of EMIC wave propagation is how the waves can reach the ground.

Extending the previous full-wave simulations [11], we examine the LHP EMIC wave propagation in dipole magnetic fields and perform a numerical survey, as shown in Figure 2(a-f). Here, we consider the effect of heavy ion density and a wave normal angle (WNA), the angle between the wavevector ($\mathbf{k}$) and $\mathbf{B}_0$, at the source. The LHP EMIC waves with wave frequency ($f = 0.45$Hz) between the local H^+ and He^+ gyrofrequencies are launched at the magnetic equator at 6.6 R_E. Figure 2 plots the simulated ellipticity for (a-c) WNA=30° and He^+ = 0, 1, and 5% plasmas and (d-f) He^+ = 5% plasmas and WNA = 0°, 45°, and 60°.

When He^+ ion density increases in Figure 2(a-c), the cutoff condition for the field-aligned waves shifts toward the outer magnetosphere and lower magnetic latitude, and the wave stopgap between cutoff and resonance locations becomes wider. As a result, waves can reach the ground for 0% He^+, while significant energy of waves reflected near the He^+ gyrofrequency for 1% He^+. For 5% He^+ in Figure 12(c), no wave can reach the ground.

Wave solutions in Figure 2(c-f) show a dependence of WNA on EMIC wave propagation. As the WNA increases, waves are dramatically changed. For WNA = 0° and 30° in Figure 2(c-d), no waves can tunnel through the wave stopgap between the LHP wave cutoff and heavier ion cyclotron frequency. For WNA = 45°, when the LHP waves obliquely incident a region where wave frequency matches the crossover frequency, mode conversion and polarization reversal from LHP to right-handed polarized (RHP) waves occur; thus, these RHP EMIC waves can propagate to the inner magnetosphere, as shown in Figure 2(e). Mode coupling between RHP and shear Alfvén waves also occurs near Earth, and these linearly polarized waves can finally reach the ground. For the large WNA case in Figure 2(f), most RHP waves propagate toward the magnetic equator, and wave power reaching the ionospheric altitude is negligible. Therefore, the results suggested that LHP EMIC waves generated near the magnetic equator with limited WNA can only reach the ground.

The EMIC waves are often generated in the outer magnetosphere at the Shabansky orbits [25] around local minima in $|\mathbf{B}_0|$ [26]. Vines et al. [27] recently showed that when the MMS satellite passed through an off-equator EMIC wave source region associated with the local $|\mathbf{B}_0|$, the Poynting vector direction systematically changed from parallel

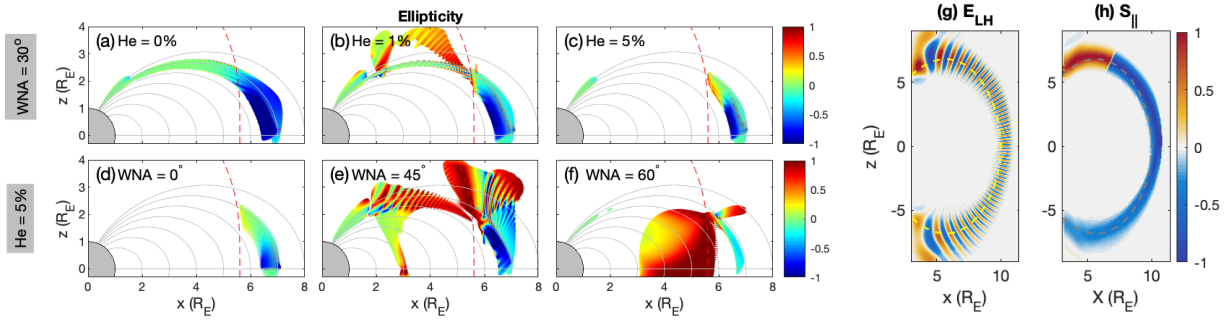

FIGURE 2: EMIC wave simulations in (a-f) dipole and (g-h) compressional magnetic fields. (a-c) WNA = 30° and He^+ = 0, 1, and 5 %. For 30° WNA, EMIC waves cannot propagate in >1% He^+. Here, red lines indicate the He^+ cyclotron frequency. The color bars show the ellipticity of EMIC wave launched as LH polarized waves at the equator, and Red (+) and blue (-) colors are right- and left-handed polarization; (d-f) 5% He^+ plasma for WNA = 0, 45, and 60°, respectively. While EMIC waves with 0° and 30° WNA are reflected at the LHP cutoff location, RHP EMIC waves with 45° and 60° WNA can reach the ground or the magnetic equator at lower L-shells; (g-h) LHP electric field and field-aligned Poynting flux. Wave amplitude and Poynting flux are normalized to the maximum values, respectively. Waves launched near $(x,z) = (7,7)\mathrm{R_E}$ at $L = 10$, and the yellow dashed line in Figure 2(g) represent magnetic field line at $L = 10$.

to the magnetic field (toward the equator), to bidirectional, to anti-parallel (away from the equator). These changes coincided with the source location shift in the southern hemisphere from poleward to equator-ward of MMS.

We adopt the compressed magnetic field configuration using the Stern model, as shown in Figure 1(b), to consider the wave propagation from the Shabansky orbit. In this case, we launch LHP EMIC waves between the local H^+ and He^+ gyrofrequencies at the $|B_0|$ minimum near $(x,z) = (7,7)\mathrm{R_E}$ in the northern hemisphere. Figure 2(g) shows the LHP component of the perturbed electric field. The launched waves in the northern hemisphere can be strongly guided by $\mathbf{B}_0$ and reach the southern hemisphere. Thus, the Poynting flux can be parallel, bi-directional, or anti-parallel to the background magnetic field depending on the location, as shown in Figure 2(h), and this shows good agreement with the recent wave observation [27].

Alfvén wave propagation

This section examines the Alfvén wave propagation in the various magnetic field shapes. By adopting the MAG2D magnetic field model, as shown in Figure 1(c-d) and the plasma density model described in Section 2, we launch a compressional wave in E_ϕ in the Pc 5 frequency range ($\sim$ mHz) at the magnetic equator at $L = 10$.

Figure 3(a-b) presents the electric field perpendicular to the local magnetic field line (E_η) representing the shear Alfvén waves. In these cases, since the waves have long wavelengths, the shear Alfvén waves globally oscillate, which is the characteristic of the field line resonance. These figures show that the field line resonance can occur in a compressed or stretched magnetic field configuration. Therefore, it is confirmed that the incorporation of the Petra-M and MAG2D is succeeded.

We also adopt realistic magnetospheric magnetic field geometries derived from global MHD simulations, as shown in Figure 1(e-f). We selected the night side of the magnetosphere, where the magnetic field is stretched to the magnetotail. Then, we also launched the compressional waves in E_ϕ at the magnetotail by assuming a substorm. Figure 3(c) shows that E_η presents field-aligned propagating waves, which are shear Alfvén waves. These waves are generated via mode conversion from the compressional Alfvén waves at the Alfvén resonance.

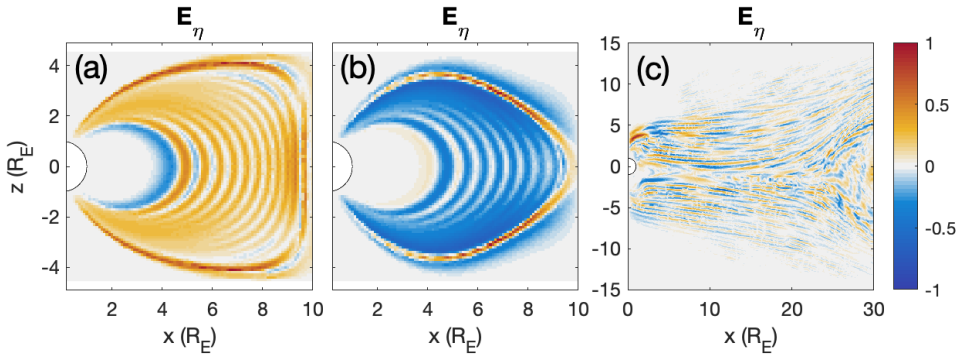

FIGURE 3: Mode-converted shear Alfvén waves appear in a transverse electric field component (E_η) in the compressional, stretched, and magnetic field in the magnetotail, as shown in Figure 1(c-f). Here, wave amplitudes are normalized to their maximum value.

CONCLUSION

This paper adopts the state-of-art Petra-M code into the Earth's magnetospheric environment. Despite the spatial scale differences between the fusion devices and Earth's magnetosphere, the Petra-M code successfully demonstrates plasma wave propagation. Due to the advantage of the FEM method, we can particularly adopt various magnetospheric equilibrium models, such as the Stern model or the MAG2D, and more realistic magnetic configurations from the global MHD model.

As examples, we demonstrate EMIC and Alfvén waves in the magnetosphere. The simulations show that the LHP EMIC waves can propagate from the source region (i.e., magnetic equator) to the ionospheric altitudes in the limited WNA when heavier ion density is less than 1%. However, since this study only demonstrates a single wave frequency, examining waves with various frequencies is necessary.

We also found that the polarization reversal at the crossover is critical for LHP wave propagation from the magnetic equator to the ground. Kim and Johnson [28] recently also showed that mode conversion and polarization are critical to externally driven RHP wave (from solar wind) propagation to the inner magnetosphere. Therefore, crossover frequency makes wave propagation from the outer magnetosphere into the inner magnetosphere independent of wave polarization at the source location.

The simulated Alfvén waves demonstrated the mode-conversion at the Alfvén resonance clearly. However, Although we successfully demonstrated the ULF wave propagation in this paper, this work adopts a simplified density model focused on the outer magnetosphere. Therefore, further study using a more realistic electron density profile, such as the global core plasma model (GCPM) [29], should be followed.

ACKNOWLEDGMENTS

This material is based upon work supported by the U.S. Department of Energy, Office of Science, Office of Fusion Energy Sciences under contract DE-AC02-09CH11466 and SciDAC Grant AT1030200. This research also used resources of the National Energy Research Scientific Computing Center (NERSC), a U.S. Department of Energy Office of Science User Facility located at Lawrence Berkeley National Laboratory, operated under Contract No. DE-AC02-05CH11231. The authors acknowledge support from NASA grants 80HQTR18T0066, 80HQTR19T0076, NNX17AI50G, 80NSSC19K0270, and 80NSSC22K0515 and NSF AGS grant 2131013.

REFERENCES

1. S. R. Elkington, M. K. Hudson, and A. A. Chan, "Resonant acceleration and diffusion of outer zone electrons in an asymmetric geomagnetic field," Journal of Geophysical Research **108**, 1116 (2003).

2. J. R. Johnson and C. Z. Cheng, "Stochastic ion heating at the magnetopause due to kinetic alfven waves," Geophysical Research Letters **28**, 4421–4424 (2001).
3. P. A. Damiano, E. H. Kim, J. R. Johnson, and P. Porazik, "Electron Energization by Parallel Electric Fields in Poloidal Standing Waves," Journal of Geophysical Research (Space Physics) **124**, 6691–6700 (2019).
4. J. L. Rauch and A. Roux, "Ray tracing of ULF waves in a multicomponent magnetospheric plasma - Consequences for the generation mechanism of ion cyclotron waves," Journal of Geophysical Research **87**, 8191–8198 (1982).
5. D.-H. Lee and R. L. Lysak, "Magnetospheric ulf wave coupling in the dipole model - the impulsive excitation," Journal of Geophysical Research **94**, 17097–17103 (1989).
6. R. L. Lysak, C. L. Waters, and M. D. Schiffer, "Modeling of the ionospheric Alfvén resonator in dipolar geometry," Journal of Geophysical Research **118**, 1514–1528 (2013).
7. R. E. Denton, "Electromagnetic ion cyclotron wavefields in a realistic dipole field," Journal of Geophysical Research: Space Physics **123**, 1208–1223 (2018), https://agupubs.onlinelibrary.wiley.com/doi/pdf/10.1002/2017JA024886.
8. P. A. Damiano, J. R. Johnson, and C. C. Chaston, "Ion temperature effects on magnetotail Alfvén wave propagation and electron energization," Journal of Geophysical Research (Space Physics) **120**, 5623–5632 (2015).
9. E.-H. Kim, J. R. Johnson, and D.-H. Lee, "Electron inertial effects on linearly polarized electromagnetic ion cyclotron waves at Earth's magnetosphere," Journal of Geophysical Research: Space Physics **124**, 2643–2655 (2019), https://agupubs.onlinelibrary.wiley.com/doi/pdf/10.1029/2019JA026532.
10. J. R. Johnson and C. Z. Cheng, "Can ion cyclotron waves propagate to the ground?" Geophysical Research Letters **26**, 671–674 (1999).
11. E.-H. Kim and J. R. Johnson, "Full-wave modeling of emic waves near the He^+ gyrofrequency," Geophysical Research Letters **43**, 13–21 (2016), https://agupubs.onlinelibrary.wiley.com/doi/pdf/10.1002/2015GL066978.
12. E.-H. Kim, J. R. Johnson, E. Valeo, and C. K. Phillips, "Global modeling of ULF waves at Mercury," Geophysical Research Letters **42**, 5147–5154, doi:10.1002/2015GL064531 (2015).
13. E.-H. Kim, N. Bertelli, J. Johnson, E. Valeo, and J. Hosea, "2D full-wave simulation of waves in space and tokamak plasmas," in *European Physical Journal Web of Conferences*, European Physical Journal Web of Conferences, Vol. 157 (2017) p. 02005.
14. E.-H. Kim, N. Bertelli, M. Ono, E. J. Valeo, J. C. Hosea, and R. J. Perkins, "Effect of wall boundary on the scrape-off layer losses of high harmonic fast wave in NSTX and NSTX-U," Physics of Plasmas **26**, 062501 (2019), https://doi.org/10.1063/1.5091579.
15. D. Stern, "Geomagnetic euler potentials," Journal of Geophysical Research **72**, 3995–4005 (1967), https://agupubs.onlinelibrary.wiley.com/doi/pdf/10.1029/JZ072i015p03995.
16. C. Z. Cheng, "Magnetospheric Equilibrium with Anisotropic Pressure," Journal of Geophysical Research **97**, 1497 (1992).
17. K. S. Park, D.-Y. Lee, M. J. Kim, C. R. Choi, R. S. Kim, K. Cho, K.-C. Choi, and J. Kim, "Global three-dimensional simulation of the Earth's magnetospheric and ionospheric responses to small-scale magnetic flux ropes in the solar wind," Journal of Geophysical Research: Space Physics **123**, 6307–6325 (2018), https://agupubs.onlinelibrary.wiley.com/doi/pdf/10.1029/2018JA025240.
18. S. Shiraiwa, T. Fredian, J. Hillairet, and J. Stillerman, "πscope: Python based scientific workbench with mdsplus data visualization tool," Fusion Engineering and Design **112**, 835–838 (2016).
19. S. Shiraiwa, J. C. Wright, P. T. Bonoli, T. Kolev, and M. Stowell, "RF wave simulation for cold edge plasmas using the MFEM library," in *European Physical Journal Web of Conferences*, European Physical Journal Web of Conferences, Vol. 157 (2017) p. 03048.
20. N. Bertelli, S. Shiraiwa, G. J. Kramer, X. Yang, T. DeHaas, C. Lau, B. V. Compernolle, E.-H. Kim, and J. C. Wright, "3D full wave fast wave modeling with realistic antenna geometry and SOL plasma," AIP Conference Proceedings **2254**, 030001 (2020).
21. N. Bertelli, S. Shiraiwa, and M. Ono, "3D full wave fast wave modeling with realistic HHFW antenna geometry and SOL plasma in NSTX-U," Nuclear Fusion (2022), https://iopscience.iop.org/article/10.1088/1741-4326/ac9690.
22. S. Shiraiwa, N. Bertelli, W. Tierens, R. Bilato, J. Hillairet, J. Myra, H. Kohno, M. Poulos, and M. Ono, "Magnetic potential based formulation for linear and non-linear 3D RF sheath simulation," Nuclear Fusion **63**, 026024 (2023), publisher: IOP Publishing.
23. R. E. Denton, K. Takahashi, I. A. Galkin, P. A. Nsumei, X. Huang, B. W. Reinisch, R. R. Anderson, M. K. Sleeper, and W. J. Hughes, "Distribution of density along magnetospheric field lines," Journal of Geophysical Research **111**, 04213 (2006).
24. S.-J. Noh, H. Kim, M. Lessard, M. Engebretson, V. Pilipenko, E.-H. Kim, J. Johnson, I. Kuzichev, and M. Salzano, "Statistical study of emic wave propagation using space-ground conjugate observations," Journal of Geophysical Research: Space Physics **127**, e2022JA030262 (2022).
25. V. P. Shabansky, "Some Processes in the Magnetosphere," Space Science Reviews **12**, 299–418 (1971).
26. R. C. Allen, J.-C. Zhang, L. M. Kistler, H. E. Spence, R.-L. Lin, B. Klecker, M. W. Dunlop, M. André, and V. K. Jordanova, "A statistical study of EMIC waves observed by Cluster: 1. Wave properties," Journal of Geophysical Research Space Phys. **120**, doi:10.1002/2015JA021333. (2015).
27. S. K. Vines, R. C. Allen, B. J. Anderson, M. J. Engebretson, S. A. Fuselier, C. T. Russell, R. J. Strangeway, R. E. Ergun, P. A. Lindqvist, R. B. Torbert, and J. L. Burch, "Emic waves in the outer magnetosphere: Observations of an off-equator source region," Geophysical Research Letters **46**, 5707–5716 (2019).
28. E.-H. Kim and J. R. Johnson, "Magnetic tilt effect on externally driven electromagnetic ion cyclotron (EMIC) waves," Geophysical Research Letters **50**, e2022GL101544 (2023).
29. D. L. Gallagher, P. D. Craven, and R. H. Comfort, "Global core plasma model," Journal of Geophysical Research **105**, 18,819. (2000).